The Role of Gravity Waves in the MLT Inversion Layers over Low-Latitude Using SABER Satellite Observations

Chalachew Lingerew[1*], U. Jaya Prakash Raju[1]

[1] Department of Physics, Washera Geospace, and Radar Science Laboratory, Bahir Dar University, Bahir Dar, Ethiopia

Correspondence to: Chalachew Lingerew (chalachewlingerew@gmail.com)

Abstract

The Mesosphere transitional region is a distinct and highly turbulent zone of the atmosphere. A transition mesosphere region is connected with dynamic processes, particularly gravity waves, as a causative of an inversion phenomenon. Understanding MIL (mesosphere inversion layer) phenomena is important under the influence of atmospheric waves for the understanding of middle and upper atmosphere dynamics for two primary reasons: stability and energy transfer. Mesospheric inversions have been the subject of numerous investigations, but their formation mechanisms are still poorly understood. In this article, an attempt has been made to investigate the upper and lower inversion phenomena and their causative mechanisms using long-term SABER observations in the height range of 60-100 km from 2005 to 2020 over a low-latitude region (3-15^0 N). The results indicate that the frequency of occurrence rate for the upper inversion is below 40%, whereas for the lower inversion, it is below 20%, indicating that the upper inversion is dominant over the lower inversion. The upper inversion exists in the height range of 78-91 km with an inversion amplitude of ~20-80 k and a thickness of ~3-12 km, whereas the lower inversion is confined in the height range of 70-80 km with an inversion amplitude of ~10-60 k and a thickness of ~4-10 km. Therein the gravity wave indicator potential energy depicts high energy (below 100 J/kg) in the upper mesosphere region (85 and 90 km) compared to the lower mesosphere region (70 and 75 km) with less than 50 J/kg. On account of Gws, the stability criteria from Brunt-Vaisala frequency (N^2) indicate instability in the upper mesosphere region with very low values relative to the lower mesosphere region. This result leads us to the conclusion that a high amount of gravity wave potential energy is a consequence of the high instability in the upper inversion relative to the lower inversion.

Keywords. MLT, Upper and Lower Inversions, Perturbed temperature, Causative gravity waves, Potential Energy, Brunt-Vaisala frequency, Instability.

Introduction

The mesosphere dynamic regions act as a transition zone to the lower and upper atmospheric wave processes (tidal waves, planetary waves, and gravity waves). It is a well-known fact that atmospheric waves, especially gravity waves (GWs) generated from the lower atmosphere, propagate into the middle and upper atmospheres, break in the mesosphere region during propagation, and dissipate their energy and momentum into the background atmosphere, influencing the dynamics of the mesosphere thermal structure, global atmospheric circulation, variability, and even the MIL phenomenon (Lindzen, 1981; Holton, 1983). The mesospheric inversion layers (MILs) are a common feature that appeared to increase the mesosphere temperature variability. The MIL is a symptom (sign) of wave saturation in the mesosphere when the lapse rate is less than half of the dry adiabatic lapse rate (Sica et al., 2007). Temperature inversions have been omnipresent features in the mesosphere regions for decades, and they have been comprehensively studied in the past by using all sorts of available techniques (e.g., lidar, radar, rocket sonde, and satellite) over different geographic locations.

Because of gravity waves (GWs) momentum and energy deposition, it is thought to be the principal mechanism driving large-scale circulation and coupling of distinct atmospheric layers, as well as inversion phenomena (Fritts and Alexander, 2003; Lindzen, 1981; Smith, 2012). In addition, the gravity wave-breaking influence on mesosphere dynamics is an attempt to demonstrate the emergence of the inversion phenomenon over mid and high latitudes (Gan et al., 2012; Walterscheid and Hickey, 2009; Collins et al., 2011; Szewczyk et al., 2013). Observational and modeling approaches have been used to investigate GWs as the causative of inversions (Fritts, 2018; Collins et al., 2014; Sridharan et al., 2008; Ramesh and Sridharan, 2012; Ramesh et al., 2013, 2014, 2017). The effect of gravity waves in the mesosphere inversion based on temperature variability is studied particularly over the mid- and high-latitudes (Singh and Pallamraju, 2018; Fritts et al., 2018). As a result, the inversion phenomenon has been the topic of numerous studies in mesosphere dynamics, yet the mechanisms of development have been poorly understood.

MILs are actual geophysical phenomena, and the study of MILs is important for a full understanding of the structure and dynamics of the MLT parts of the upper atmosphere (Meriwether and Gardner, 2000; Meriwether and Gerrard, 2004). Regarding the low latitudes, there are very less number of studies on the temporal (time) and spatial (altitudinal, latitudinal, and longitudinal) variability of the mesosphere inversion phenomenon associated with gravity wave

activity. This motivates us to investigate the mesosphere inversion phenomenon and its association with gravity wave activity, along with stability criteria using Brunt-Vaisala frequency (N^2) over the low latitudinal band (3-15^0 N) using long-term SABER observations during 2005-2020. This is organized as follows: The data and method of extracting the mesosphere inversion phenomenon are presented in Section 2, and their results are described in Section 3. Finally, Section 4 presents the conclusions.

2. Observation and Data analysis

2.1 SABER Observation

The TIMED/SABER satellite was launched on December 7, 2001, to set on an elliptical orbit at an altitude of about 625 km with an inclination of 74^0 from the equator. The SABER instrument makes 15 orbits; each orbit takes 97 minutes (1.6 h) and provides about 1400 profiles per day; each profile takes 58 seconds. This TIMED/SABER satellite provides temperature profiles with good spatial and temporal resolution to investigate mesosphere dynamics and their atmospheric wave processes. SABER temperature data has been widely used to investigate the typical thermal structure and dominant dynamical processes in the mesospheric region (Garcia et al., 208, Gan et al., 2012, 2014; Bizuneh et al., 2022; Lingerew et al., 2023). For vertical temperature measurement, SABER provides an accuracy of 1 to 2 K between 15 and 60 km, decreasing to 5 K below 85 km, while the error increases with altitude from 6.7 K to 10 K near 100 km (Rezac et al., 2015). In the current work, we have used the latest version 2.0 of SABER observed temperature data over low latitudes. The SABER vertical temperature profiles in the region of 60-100 km altitude during the period January 2005-December 2020 over (3-15^{0}N) latitude and (33-48^{0}E) longitude regions are used. Based on the monthly mean SABER profile data the mesosphere and lower thermosphere (MLT) variability is presented, as shown in Figure 1. The monthly mean temperature of the mesosphere region (60-100 km) shows a maximum temperature of 200-240 K in the height range of 60-70 km, with the minimum temperature declining to around 160-180 K in the height range of about 95-100 km throughout all over the period.

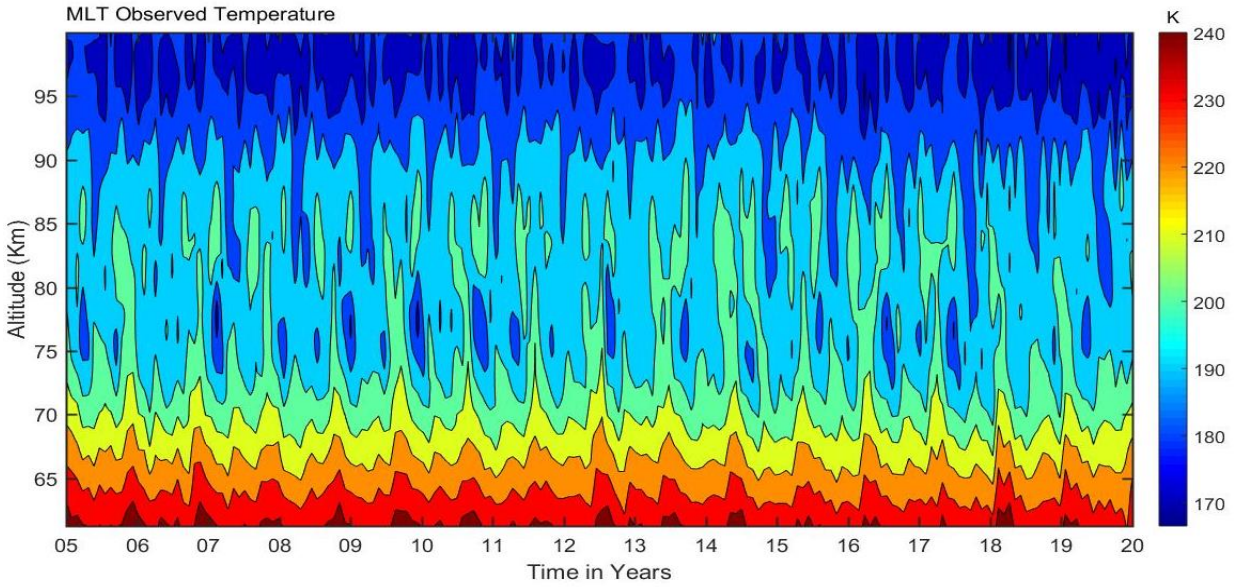

Figure 1. The monthly mean MLT temperature variability in the height range of 60-100 km during December 2005-January 2020 over the low-latitude.

2.2 Analysis Technique

Mesosphere inversions of temperature are identified based on their characteristics thickness, and amplitude corresponding to an altitude and temperature difference between the top and bottom levels. In this investigation, the upper and lower mesosphere inversions are identified using the following criteria: (1) The bottom level of the lower and upper inversions is above 70 and 80 km, and its top level of inversion is below 80 and 92 km, respectively; (2) the amplitude is considered larger than 5 K; and (3) the thickness is greater than or equal to 2 km following the procedure. As well as identifying the inversions based on the above criteria, the upper and lower MLT inversion occurrence rate or percentage is derived by counting the number of inversion days in every month from 2005 to 2020. Inversions that satisfy the above-mentioned criteria are considered significant. Based on this sequence of temperature inversion, diagnostic techniques provided in the methodology (e.g. Gan et al., 2012 and Sivakandan et al. 2014) were applied to the SABER observed data during the period 2005-2020 over low latitudes to investigate the causative influence atmospheric gravity waves (Gws). This inversion of the mesosphere temperatures is related to their instabilities. Hence, we are going to derive the hourly atmospheric gravity waves via the Brunt-Vaisala frequency (N^2).

Another important concept to estimate the Brunt-Vaisala frequency is the potential temperature (θ), which stands for the air parcel's temperature when it is displaced adiabatically to a standard pressure level, p_0, from the current pressure level, p, based on the first law of thermodynamics:

$$\frac{dT}{T} = \frac{R}{c_p}\frac{dp}{p} \Rightarrow \quad \int_T^0 \frac{dT}{T} = \int_p^{p_0} \frac{R}{c_p}\frac{dp}{p} \qquad (1)$$ it yields

$$\theta = T\left(\frac{p_0}{p}\right)^{R/c_p} \qquad (2)$$

Therefore, the motion of the vertical atmospheric air parcel can be described by (Liu, 2011; Vadas and Fritts, 2005) as follows in equation (2.3) to calculate the Brunt-Vaisala frequency of the parcel due to the Buoyant and gravitational forces acting on the parcel:

$$\frac{d^2s}{dt^2} = -\mathrm{g}\frac{\rho-\rho_0}{\rho}\, sina \qquad (3)$$

Based on the hydrostatic equation, $\rho = \rho_0$, and $p = p_0 \Rightarrow \frac{\partial p}{\partial z} = \frac{\partial p_0}{\partial z} = -\mathrm{g}\rho_0$ (4) and the ideal gas law, $\rho = p/RT = p_0/RT$ gives the parcels motion of an equation:

$$\frac{d^2s}{dt^2} = -\frac{\mathrm{g}}{\rho}\left(\frac{d\rho}{dp}\frac{\partial p_0}{\partial z} - \frac{\partial \rho_0}{\partial z}\right)z \qquad (5)$$

Following the same approach using the hydrostatic equation (4) and adiabatic equation (6)

$$dln\rho = \frac{dlnp}{\gamma}\,, \gamma = c_p/c_v \qquad (6)$$ yields

$$\frac{d^2s}{dt^2} = -\frac{\mathrm{g}}{\rho}\left(\frac{\rho}{\gamma p_0}\frac{\partial p_0}{\partial z} - \frac{\partial \rho_0}{\partial z}\right)z = \mathrm{g}\left(\frac{\partial ln\rho_0}{\partial z} - \frac{1}{\gamma}\frac{\partial lnp_0}{\partial z}\right)z \qquad (7)$$

For the ideal gas law of $p = \rho RT$, the natural logarithm is taken for altitude, z on both sides, yielding

$$\frac{\partial ln\rho}{\partial z} = \frac{\partial lnp}{\partial z} - \frac{\partial lnT}{\partial z} \qquad (8)$$

Then after, the potential temperature (θ) of the atmospheric parcel is calculated as follows based on the equation (2):

$$\frac{\partial ln\theta}{\partial z} = \frac{\partial lnT}{\partial z} - \frac{R}{c_p}\frac{\partial lnp}{\partial z} = \frac{1}{T}\left(\frac{\partial T}{\partial z} + \frac{\mathrm{g}}{c_p}\right) = \left(1 - \frac{R}{c_p}\right)\frac{\partial lnp}{\partial z} - \frac{\partial ln\rho}{\partial z} \qquad (9)$$ to derive the

Parcels acceleration based on equations (7) to become:

$$\frac{d^2s}{dt^2} = -\,\mathrm{g}\,\frac{\partial ln\theta_0}{\partial z}\, z\, sina = -\,\mathrm{g}\,\frac{\partial ln\theta_0}{\partial z}\, ds.sin^2 a \qquad (10)$$

Whereas by introducing the frequency, N, with $N^2 = \mathrm{g}\,\frac{\partial ln\theta_0}{\partial z}$

The Brunt-Vaisala frequency, N^2 is calculated based on the following mathematical formulation used to characterize atmospheric stability.

$$N^2(z) = \frac{g(z)}{T_0(z)}\left(\frac{\partial T_0(z)}{\partial z} + \Gamma_d\right) \quad (11)$$

Where g is the acceleration due to gravity, N is the Vaisala frequency, T_0 is the background temperature, estimated based on the third-order polynomial fitting, $\Gamma_d = {}^{g}/_{c_p}$ is the adiabatic lapse rate, and $c_p = 1004\, J\, K^{-1}\, kg^{-1}$ is the specific heat capacity of the atmosphere at constant pressure. When Vaisala frequency N^2, is statically positive, the atmosphere is stable. While the frequency N^2, is negative, the atmosphere is unstable, in which the atmospheric lapse rate, $\Gamma = -\frac{\partial T}{\partial z}$ is larger than the adiabatic lapse rate, ${}^{g}/_{c_p} \approx 9.5\, K\, km^{-1}$, the atmosphere is unstable.

In the meantime of estimating the Brunt-Vaisala frequency, the third-order polynomial fit of the least squares has been applied to the SABER observed temperature (T) profile to estimate the background temperature (T_0) following the procedure Leblanc and Hauchecorne (1997). Succeeding the estimations of the perturbed temperature (T_p) from equation (2), the impacts of gravity waves based on the potential energy (P_E) on the mesosphere and lower thermosphere (MLT) temperature variability were identified, which is estimated by subtracting the background from the observed temperature data (T).

$$T_p = T - T_0 \quad (12)$$

After estimating the perturbed temperature (T_p), a 1-hour interval of the cut-off frequency of the low-pass band filter is used to remove the planetary and tidal wave contributions in the perturbed temperature or signal data above in one-hour time intervals to extract the impacts of a one-hour interval of gravity waves (short-periods). Then after applying the low pass band filter on the perturbed temperature (Tp), the atmospheric gravity wave of potential energy (E_P) is estimated (John and Kumar, 2012) based on the Brunt-Vaisala frequency.

$$E_p(z) = \frac{1}{2}\left(\frac{g(z)}{N(z)}\right)^2 \left(\frac{T_p(z)}{T_0(z)}\right)^2 \quad (13)$$

The potential energy of the waves is a function of altitude, z, which is utilized to determine the impact of atmospheric gravity waves on atmospheric dynamics.

3. Results and discussion

3.1 Identification and Characteristics of the Lower and Upper MLT Inversion

The daily SABER observed temperature profiles of the upper and lower mesospheres from 2005 to 2020 over low latitudes are depicted in the form of contours in Figure 2(a and c) in the range

between ~ (180-220 K). The lower panel of Figure 2(b and d) shows daily inversion temperature profiles in the range of 180–225 K, indicating temperature is maximum in the inversion day observed temperature at lower and upper regions when compared without considering the inversion day observed temperature in Figure 2(a and c).

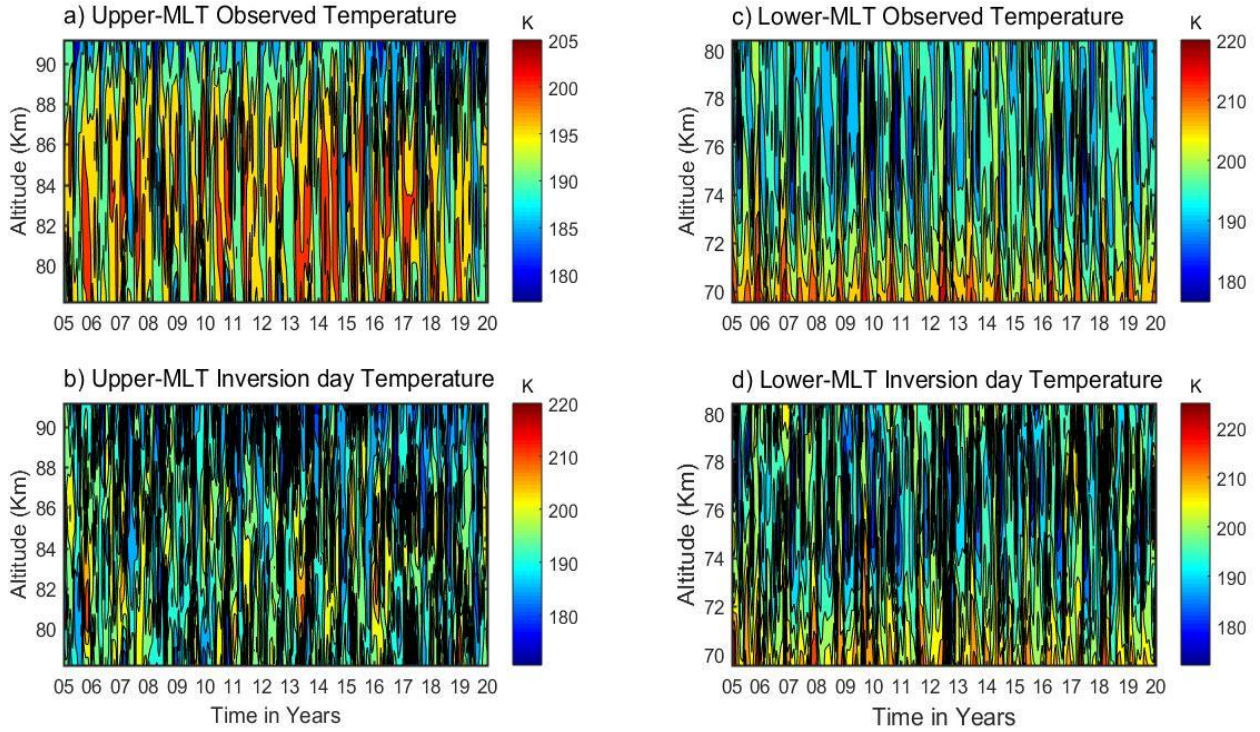

Figure 2. The upper and lower mesosphere observed temperatures in the first horizontal panel at (a and c) with their inversions in the second horizontal panel at (b and d).

The upper panel on the left side of Figure 2(a) represents the upper mesosphere observed temperature, which is depicted in the range ~(180-205 K) at the height around ~80-90 Km, and the right upper panel of Figure 2(c) represents the lower mesosphere observed temperature in the range around ~(180-220 K) at the height around ~70-80 Km. Whereas, Figure 2(b) depicts an upper-temperature inversion about ~(180-220 K) at an altitude of ~(80-90 Km), while Figure 2(d) shows a lower-temperature inversion about ~(180-225 K) at a height of ~(70-80 Km), indicating a temperature gradient is occurred from negative to positive due to external or internal drivers, which might be atmospheric gravity waves, chemical reactions or solar radiations. The first observation of MIL was carried out by a rocket-falling experiment, which shows temperature inversion layers have been normally detected with maximum values in the mesosphere and lower thermosphere (Schmidlin, 1976). Our findings of the lower inversions in the range of (70-80 km)

tend to approach the reports by Sivakumar et al. (2001), which show that the base of the lower mesospheric inversion layer (MILs) lies in the range of (73-79 km). Whereas Sivakandan et al., (2014) also investigated the lower and upper mesospheric inversions in the altitudinal regions from 60-105 km over low latitudinal regions, which nearly coincides with our work results.

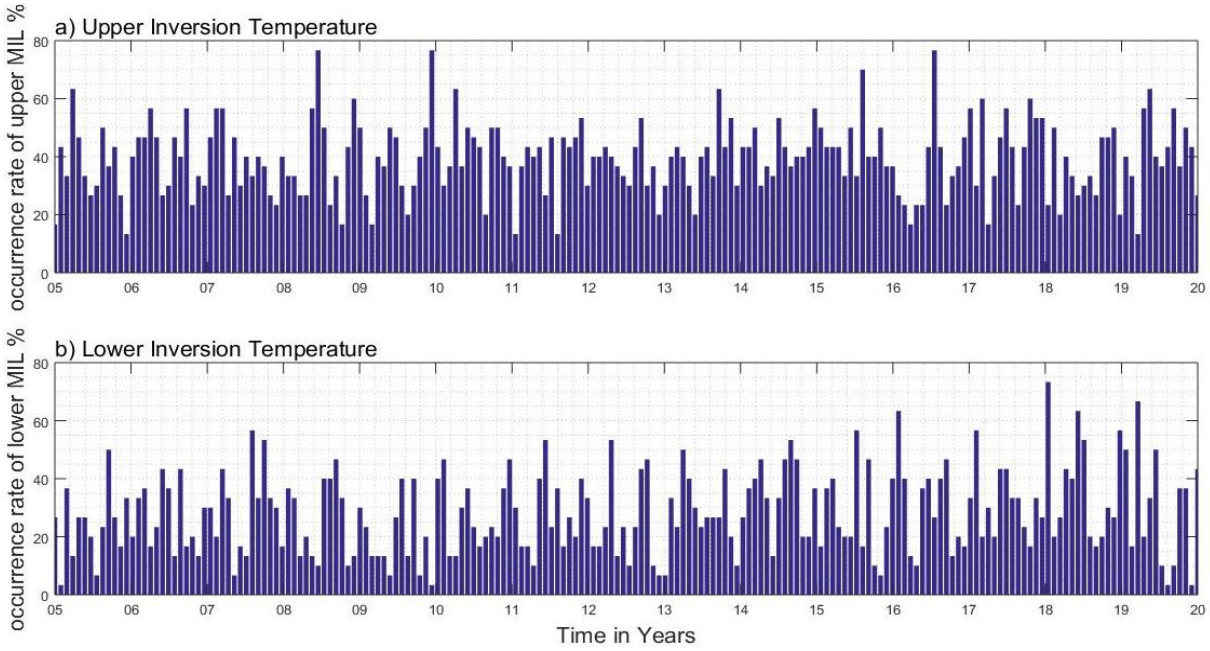

Figure 3. The frequency occurrence rate (percentage) of the (a) upper and (b) lower inversion temperatures during 2005-2020 over low latitudes.

Further, the frequency occurrence (%) of mesospheric inversion layers (MILs) is investigated during the period 2005-2020, and the results are displayed in the form of a histogram in Figure 3(a) for the upper MIL and in Figure 3(b) for the lower MIL. The mean frequency occurrence rate of the upper inversion is approximately below 40%, whereas their maximum occurrence rate of inversion lies between 60% and 78%, particularly in the years 2008, 2010, and mid-2016. While the mean frequency occurrence rate of the lower inversion is below 20%. As a whole, the occurrence rate of the upper inversion is relatively high compared with the lower inversion, which could be related to atmospheric wave activities, particularly gravity wave activity. In this regard, Hauchecorne et al. (1987) and France et al. (2015) tried to show the impacts of Gws on the upper and lower mesosphere inversion variability. Not only this, Gan et al. (2012) also found the seasonal variation of MILs in the low latitudes and the causative planetary waves on the lower MILs variability. After determining the occurrence of the inversions in the lower and upper MLT regions, their consequences should be investigated.

Before examining the effects of Gws on the MLT regions of an inversion, Figure 4 depicts the inversions of mesosphere temperature variability in terms of base height, amplitude, and thickness. The frequency occurrence of amplitude, thickness, and base height of inversion variability in the form of the histogram along with the best-fit red lines of the Gaussian distribution are presented in Figure 4. The observed distributions coincide with Gaussian curves, indicating that the number of MILs is distributed over their attributes according to normal laws, implying that the representations are real-valued random variables. In Figure 4 of the left vertical column, three rows represent a histogram of (a) amplitude, (b) thickness, and (c) the base of the upper MIL phenomenon, along with their statistical metrics mean and standard deviations (SD). Whereas the corresponding three rows of the right vertical column represent (d) amplitude, (e) thickness, and (f) the base of the lower MIL phenomenon.

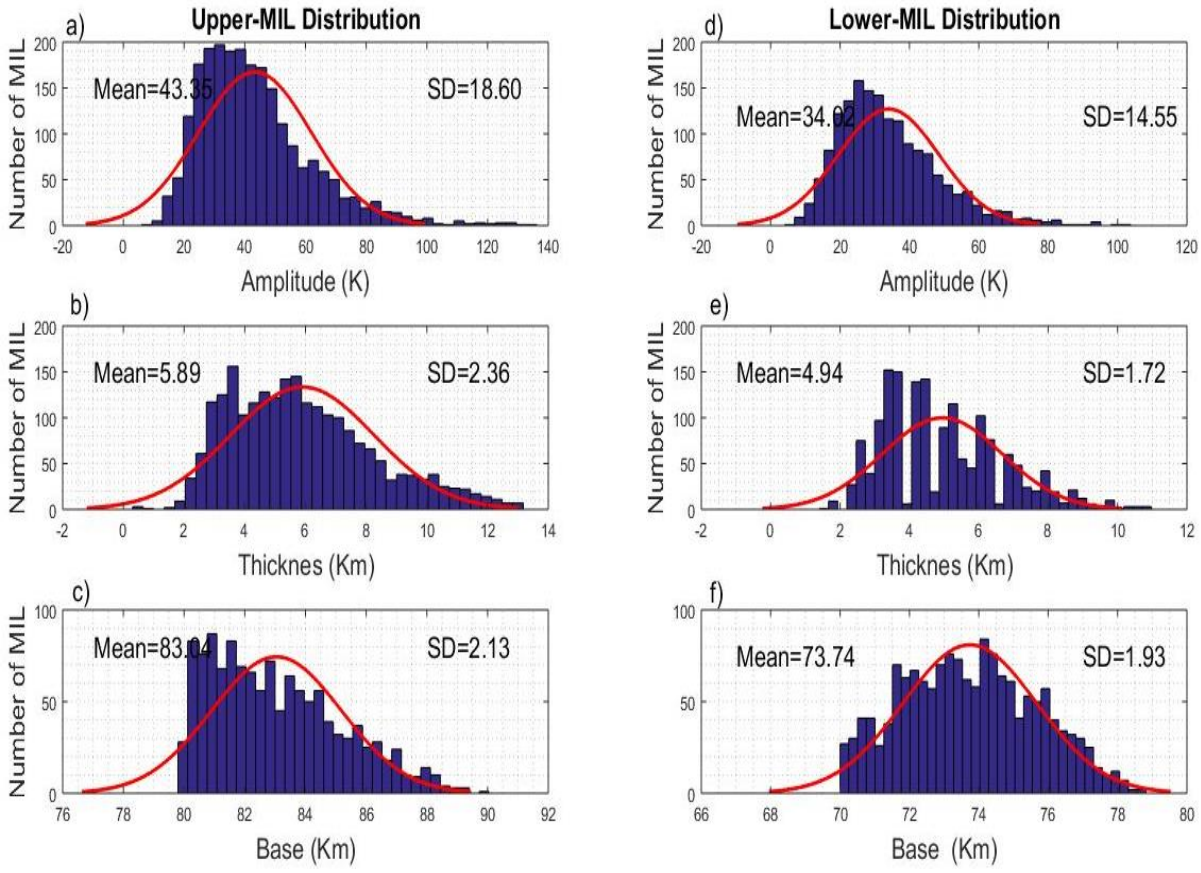

Figure 4. Histogram occurrence of mesosphere inversions. The first vertical panel represents the upper inversion distribution of (a) amplitude, (b) thickness, and (c) base, and the corresponding distribution in the second vertical panel is the lower inversion of (d) amplitude, (e) thickness, and (f) base over the low latitude during the period 2005–2020.

The amplitude of upper inversion variability in the left vertical panel in Figure 4(a) exists in the range between 20 and 80 K, with a peak value of 38 K following a Gaussian distribution with large standard deviations (SD), 18.6. The thickness of the inversion layer for upper MILs has existed in the range of 3-9 K, with the most probable value of 5.5 K and a low standard deviation (SD) of 2.3 (Figure 4(b)). The base height of the upper MIL in Figure 4(c) ranges from ~80 to 90 km, with a peak value of a large number of upper mesospheric inversions occurring at a base height of around 83 km in a lower standard deviation (SD) of 2.13. The number of upper inversions all over the period 2005–2020 at a height of 82 km is the highest relative to the rest in the range between 80 and 90 km. Such maximum mean to fit of Gaussian distribution Maybe the reason for the gravity wave breaking is that it dissipates energy as a causative factor for an inversion, while the wave generated from the lower to the upper atmospheric region as well as the impacts of the solar flux generated from the upper solar system. Whereas, the lower inversion amplitude is depicted in the range between 10 and 60 K with a peak of 25 K and standard deviations (SD) of 14.5 in Figure 4(b) in the right vertical panel. The thickness of an inversion has appeared in the range of 3-8 Km, with the most probable value of 3.8 Km and a low standard deviation (SD) of 1.72 (Figure 4(d)). The base height of the lower inversion of Figure 4(f) is in the range of 70 and 80 km, with a peak value of around 74 km, showing a lower standard deviation (SD) of 1.93. The statistical distribution presented in this work fairly coincides with the work published by Begue et al. (2017) over Reunion (20.8º S, 55.5º E) and Mauna Loa (19.5º N, 155.6º W) using Rayleigh lidar and SABER observations. For both sites, MILs are found to be distributed in the altitude range of 75 to 82 km, with a maximum amplitude above 30K.

3.2 Latitudinal Variations of Mesospheric Inversion Layers (MILs)

In this section, the spatiotemporal (latitudinal-time) variability of the upper and lower mesosphere inversion phenomena is characterized in the contour plots of time **vs.** latitude in Figures (5 and 6) respectively, based on amplitude, thickness, and base height over the low-latitude band (3-15^0 N) during 2005–2020. The Upper MILs phenomenon is observed around 80–90 km, with the maximum amplitude in the range of 90–120 K over all the latitude bands (5^0-12^0 N) during 2005, 2007, mid-2011, 2013, 2015, 2016, mid-2019, and 2020 (Figure 5(a)). The inversion thickness depicted in the second horizontal panel, as shown in Figure 5(b), is displayed with a maximum range of ~(8–12 Km) over the entire latitudinal region (3-15^0 N). Figure 5(c) displays the relative

maximum inversion base height around ~(84-88 Km) in the latitudinal range between 4 and 14^0 N during 2006, 2008, 2010, 2012, 2016, and 2018.

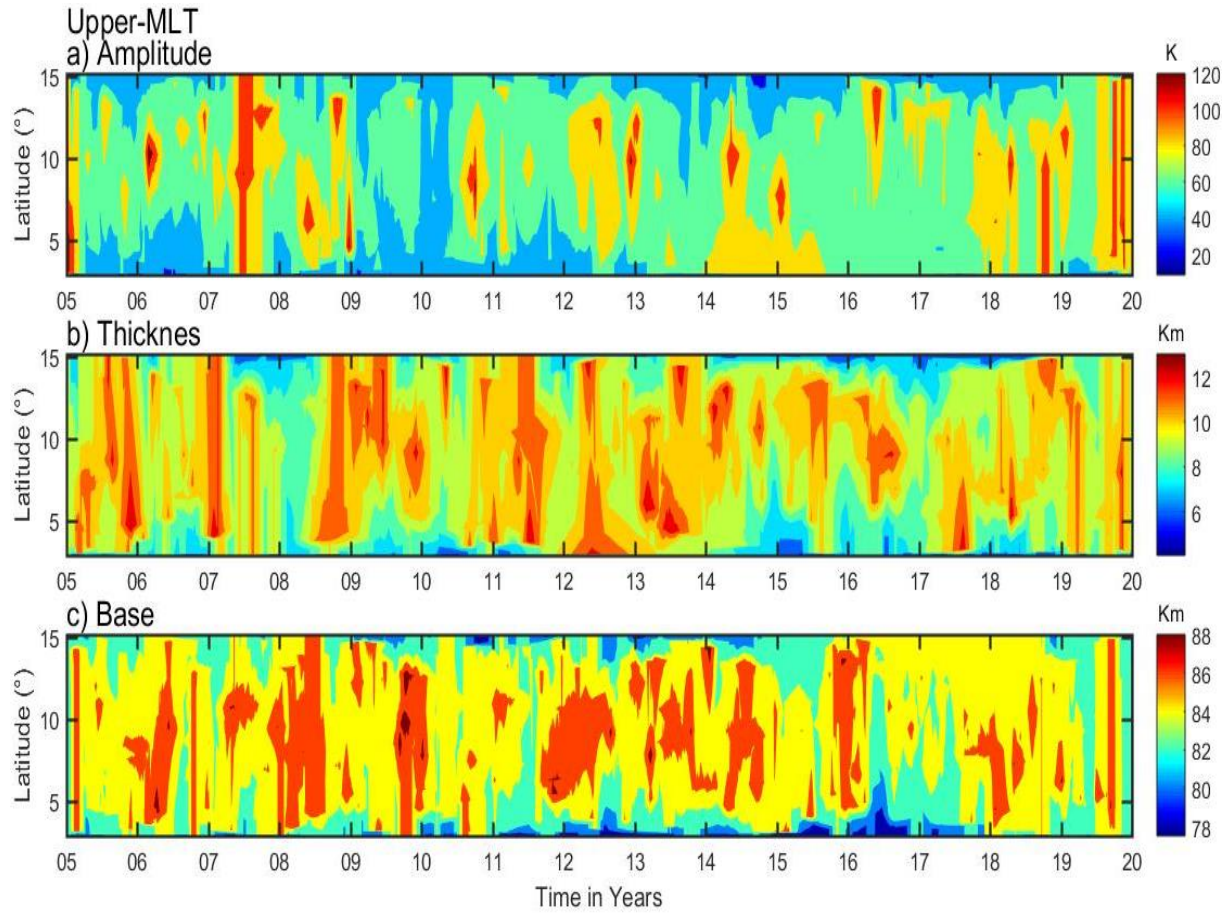

Figure 5. The daily upper inversions (~80-90 km) of (a) amplitude, (b) thickness, and (c) base height during 2005-2020 over latitudinal variation.

Similarly, the latitudinal variations of the lower inversion (MILs) phenomenon based on their characteristics amplitude, thicknesses, and base height are depicted in the form of contour plots of time **vs** latitude in Figure 6(a, b, and c), respectively, over an altitudinal range around ~(70-80 km). The lower inversion amplitude is depicted in the range of ~30-60 k over all latitudinal bands except the maximum range of ~(80-100 k) during 2013, 2015, 2016, and 2019 in different latitudinal regions enclosed in the range between 5 and 14^0 N. Figure 6(b) displays the inversion thickness of 5-7 km over the entire latitude band, except for the maximum thickness of 8-10 km. The inversion of base height (76-80) is depicted in Figure 6(c) over all latitudes and periods except 2008, 2014, and mid-year 2018 with maximum base height. Figures 5 and 6, clearly show that the high amplitude and thickness of the upper inversion in comparison with the lower inversion indicate a highly dynamic phenomenon over the upper mesosphere region.

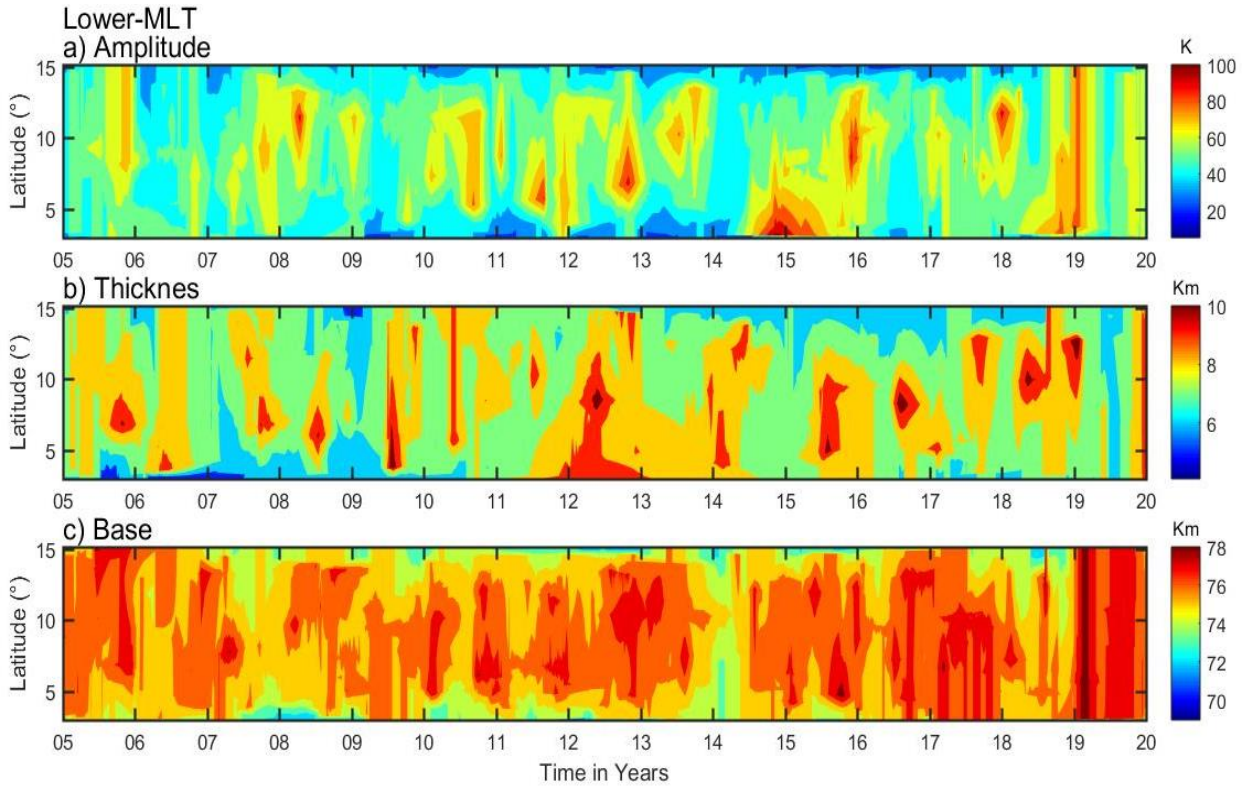

Figure 6. Same as Figure 5, but for the lower mesosphere inversions (~70- 80 km).

From Figures 5 and 6, it is observed that the upper inversion amplitude and thicknesses show high values in comparison with the lower inversion, indicating a highly dynamic phenomenon over the upper mesosphere region. Satellite measurements have a significant contribution to the information on latitudinal variations in MILs. The global climatology of MILs observed by TIMED/SABER shows that MILs also occur at low latitudes in the tropics (Gan et al., 2012).

3.3 Separations of the Perturbed Temperature in the Mesosphere Region

The perturbed temperature profiles (T_p) in the upper and lower mesosphere inversions during the period of 2005-2020 can further be used to calculate their factors' potential energy of gravity waves and the Brunt-Vaisala frequencies (N^2). The procedure for calculating perturbation temperature (T_p) is mentioned in the methodology part.

First, the upper-temperature inversion profiles are identified in the MLT region during the entire observational period of 2005-2020, as displayed in the contour plot of Figure 7(a). It is noted that the inversion temperature is in the range of ~170-220 K with less detectable variability. Based on this inversion temperature profile, the background temperature (T_0) is calculated by applying a 3rd-order polynomial fit as shown in the corresponding contour plot of Figure 7(b). This background

temperature displays identifiable periodic variability in the range of ~195-197 K around ~82-87 km. While the perturbed temperature profiles (T_p) are based on the difference between the observed inversion temperature (T) and the corresponding background temperature profiles (To), they display in the range of -25 to +25 K, as shown in Figure 7(c).

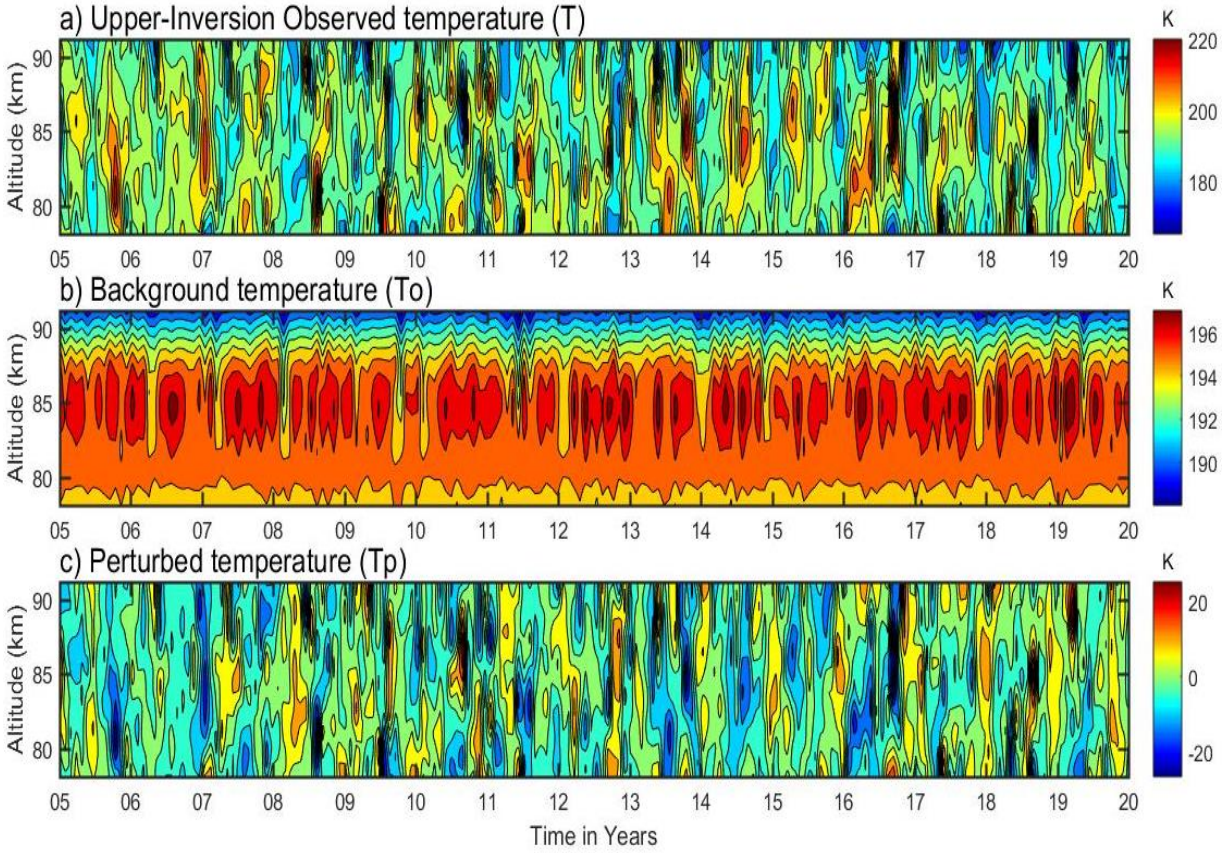

Figure 7. The upper mesosphere temperatures in the vertical panel are: (a) inversion day observed temperature; (b) background temperature; and (c) perturbed temperature in the upper mesosphere region.

A similar procedure has been applied to calculate the perturbed temperature (T_p) as well as the observed and background temperature from 2005 to 2020 in the lower mesosphere region, and their corresponding contours are displayed in Figure 8(a-c). The observed temperature of lower inversion in Figure 8(a) depicted a range of ~170-220 K and the background temperature of lower inversion in the range of ~ 195-210 K with their maximum values of ~200-210 K over the height of ~70-72 Km as shown in Figure 8(b). Whereas the perturbed temperature in Figure 8(c) is presented in the range between -25 and 20 K. It is noted that the upper mesosphere perturbed temperature is at its maximum compared to the lower mesosphere region, which may be due to a high dynamic phenomenon.

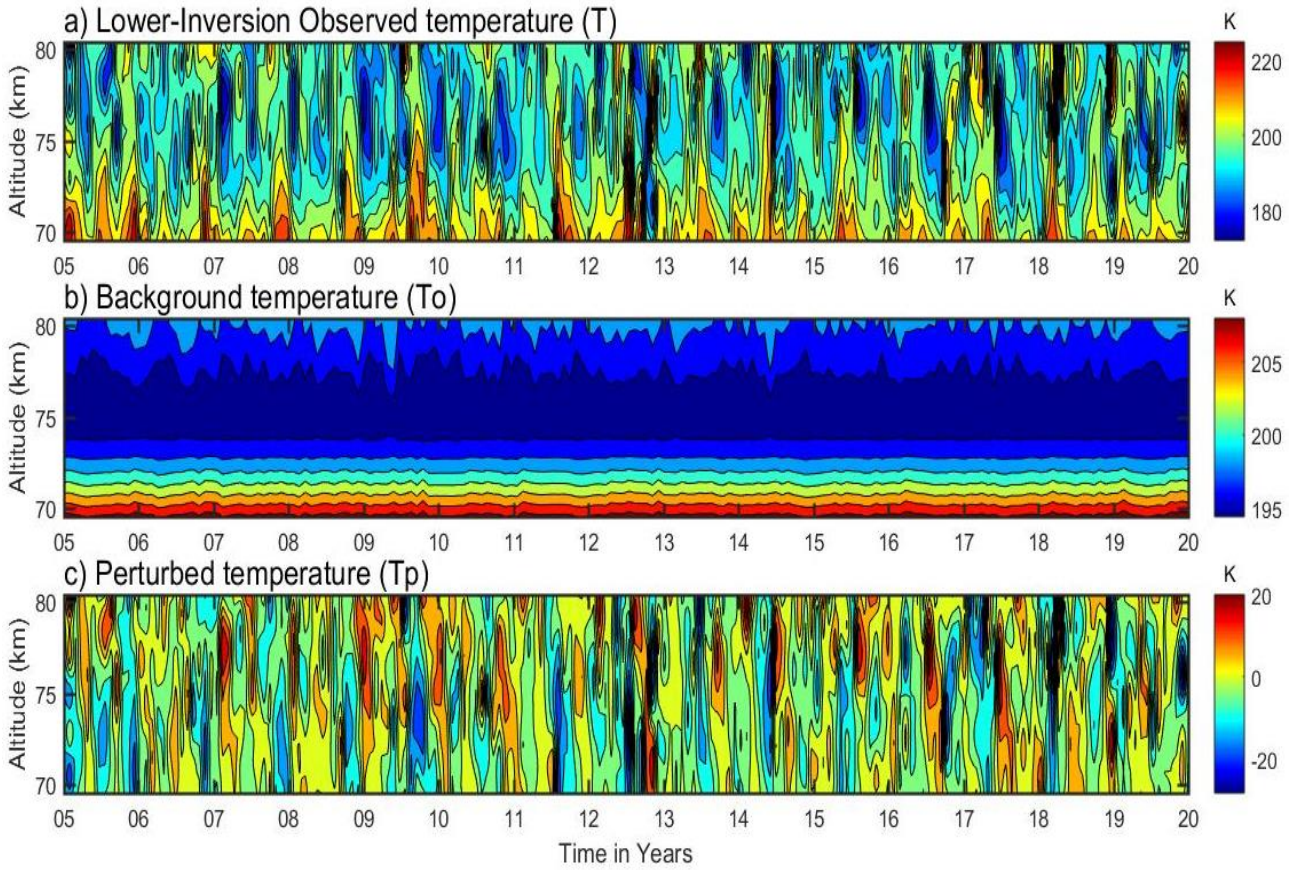

Figure 8. Same as Figure 7, but for the lower mesosphere atmospheric region.

3.4 Effects of Gravity Waves on Mesosphere Inversions and Associated Instability

Atmospheric waves (gravity waves, planetary waves, and tidal waves) exist in different layers of the atmosphere and are generated by different mechanisms. Gravity waves are of local or regional dimensions, whereas the other two waves are of global extent. This dynamical influence of gravity wave motion is a restoring force of gravity acting downward and buoyancy acting upward on vertically displaced air parcels from the troposphere/stratosphere through the upper thermosphere. These propagated gravity waves can be distributed from their source regions across the atmosphere and become saturated at the critical upper atmospheric level, particularly over the low latitudes. Thereby, the vertically propagated waves were breaking and dissipating to transfer their energy and momentum into the atmospheric background field, thus considerably affecting the structure and variability of the atmosphere, as shown in Figure 10, as well as the results of (Holton et al., 2003; Holton and Hakim, 2013) waves potential energy affecting the atmospheric temperature inversions. The saturation stage of the wave propagation is broken at the upper region to dissipate the energy,

311 which impacts the normal mesospheric temperature by increasing its temperature with elevation,
312 known as an inversion. This is the reason gravity wave potential energy is connected with an
313 inversion.
314 In this section, an attempt has been made to investigate the longitudinal variability of gravity waves'
315 contribution to the mesospheric inversions (MILs) phenomenon by calculating potential energy and
316 their instability based on Bruent-Vaisala frequency (N^2) using perturbed temperatures. Before
317 deriving the waves' potential energy from the perturbed temperature (T_p), a comparison of before
318 and after applying one-hour intervals of cut-off frequency of a low-pass band filter on a perturbed
319 temperature during the period 2005-2020 at selected heights of 90, 85, 75, and 70 km, as depicted
320 in Figure 9 (a, b, c, and d), represented by a blue line plot to remove unwanted influences on an
321 inversion. The reason behind using the low-pass band filter is to eliminate/remove the unwanted
322 influence of long-period oscillations on an inversion such as tidal or planetary waves. The effects
323 of the low-pass filter are visible before and after applying the filter in Figure 9(a and b) for the
324 upper mesosphere region at 90 and 85 km and in Figure 9(c and d) for the lower mesosphere region
325 at 75 and 70 km. The amplitude of the perturbed temperature is reduced to the range around ~(-10
326 to 10 K), and the data is smoothed by eliminating higher frequencies.

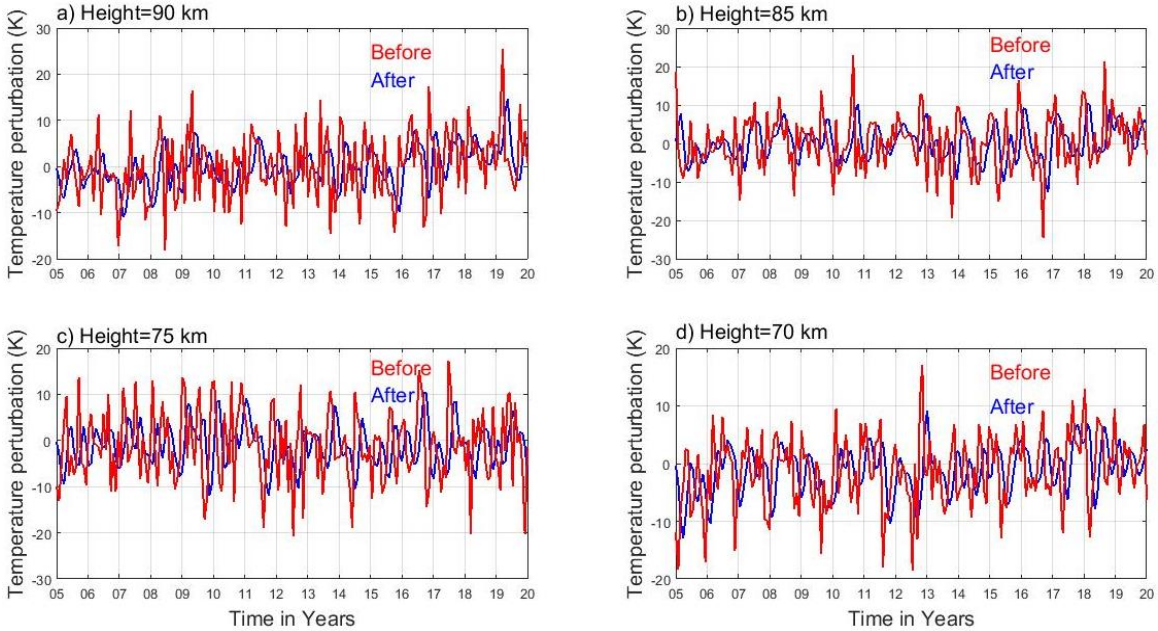

327
328 **Figure** 9. Perturbed temperature profiles before (red color) and after (blue color) applying the low-
329 pass band filter for the upper (85 and 90 km) and lower (70 and 75 km) regions.
330 By using the time series of filtered perturbed temperature data at selected heights of 90, 85, 75,
331 and 70 km, the potential energy (E_p) is constructed based on the formula mentioned in the

methodology section, since gravity wave activity is projected by potential energy calculation as described from numerous authors (Tsuda et al., 2000; Wang and Geller, 2003; Liu et al., 2014; Thurairajah et al., 2014). The spatiotemporal variability of gravity wave potential energy is shown in Figure 10(a and b) for the upper mesosphere region at (90 and 85 km) and Figure 10(c and d) for the lower mesosphere region at (75 and 70 km).

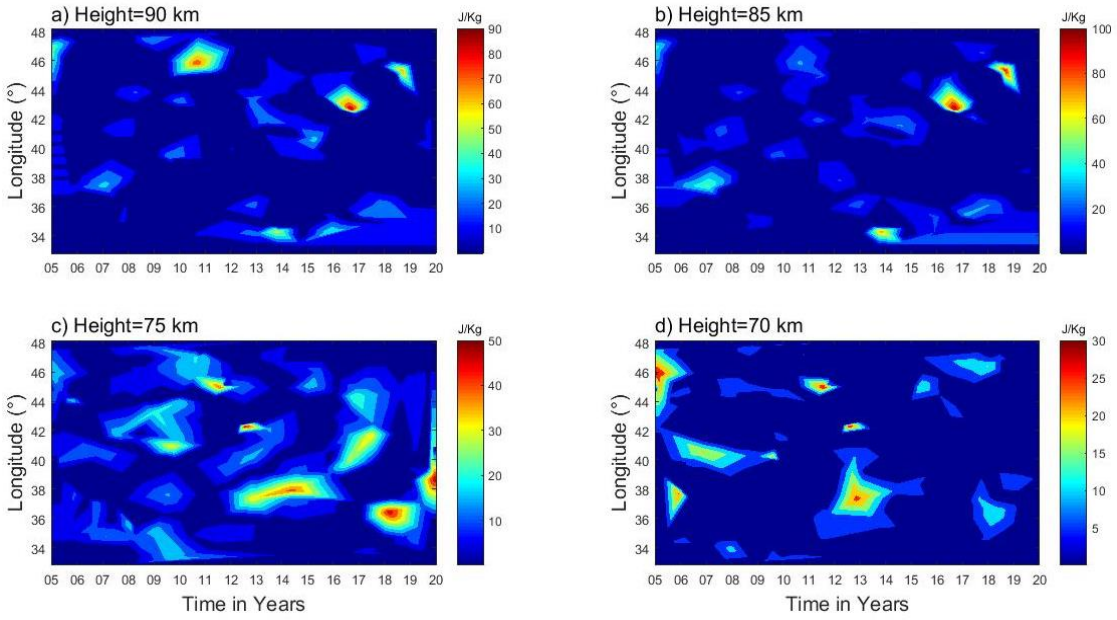

Figure 10. Gravity wave potential energy for the upper (85 and 90 km) and lower (70 and 75 km) mesosphere regions.

In this investigation, the maximum gravity wave potential energies were observed in the range of around ~70–90 J/kg over the longitudinal regions of 45-47^0 E, 43^0 E, and 44^0 E during 2011, 2017, and 2019 (Figure 10(a)) for upper mesosphere inversions at 90 km, whereas the low potential energy of gravity waves around ~10–60 J/kg is presented all over the longitudinal region from 33-48^0 E. While the maximum potential energy ~(70-100 J/kg) is observed at 85 km as shown in Figure 10(b) over the longitudinal (340, 440, and 460) regions during 2014, 2016, and 2018. The low potential energy of gravity wave between 20 and 70 J/kg appears in all the longitude (33-48) regions. However, Figures 10 (c and d) show the lower mesosphere regions of gravity wave potential energy at 75 and 70 km, respectively. At a height of 75 km, a relative maximum potential energy appeared in the range of 40-50 J/kg over the longitudinal (46^0, 42^0, 40^0, 37^0, 36^0, and 38^0) region during 2011, 2012, 2017, 2013–2015, 2018, and 2020. Similarly, Figure 10(d) depicts the gravity wave potential energy in the range of 2–30 J/kg for the lower mesosphere region at 70 km

over the longitudinal region (33-48^0). Out of which, the maximum potential energy of 25-30 J/kg is found in a certain longitude region over a while. Many possible mechanisms have been suggested for the cause of lower MIL formations, nonlinear interactions between GWs and tides (Liu and Hagan, 1998), and chemical heating (Meriwether and Mlynczak, 1995) including GW breaking (Hauchecorne et al., 1987). Liu et al., (2000) showed that breaking gravity waves can warm the air necessary for the formation of MILs. It is also understood that gravity waves, tides, planetary waves, and chemical processes are managing the middle atmospheric variability (Sivakandan et al., 2014). The role of gravity wave propagation and dissipation has been accepted as the dominant wave forcing in the MLT region (Lindzen, 1981; Holton, 1983), which affects the middle and upper atmospheric features of an inversion. Gravity waves are multi-scale in nature; small-scale waves may contribute predominantly to unstable or instability, and turbulence in the MLT dynamic region (Liu and Meriwether, 2004; Szewczyk et al., 2013).

Hence, investigating MIL phenomena is important for the understanding of MLT atmosphere dynamics for two primary reasons: stability and energy transfer. As a result, an attempt has been made to examine the contributions of gravity waves to the MLT region's instability as well as the MIL phenomenon using the Brunt-Vaisala frequency calculations described in the approach. The spatiotemporal variability of Vaisala frequency is displayed in the contour Figure 11(a and b) for the upper mesosphere region (90 and 85 km) and Figure 11(c and d) for the lower mesosphere region (75 and 70 km). Based on the Brunt-Vaisala frequency, N2, the upper MLT region is unstable (~0.027) at 90 km and (~0.029) at 85 km maximum relative to the lower inversion instability at 75 km (~0.033) and 70 km (~0.035). Hauchecorne et al., (1987) described a model in which a succession of breaking GWs would generate the MIL through the gradual accumulation of heat as a cause of instability.

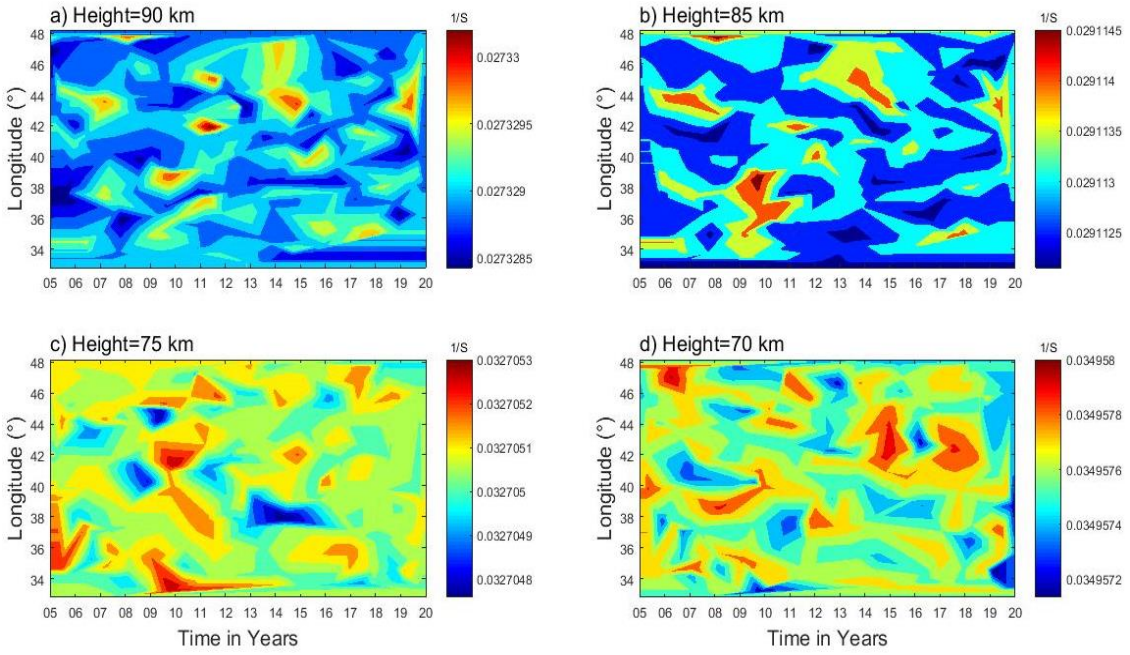

Figure 11. Brunt-Vaisala frequency (N^2) profiles for the upper (85 and 90 km) and lower (70 and 75 km) mesosphere regions.

4. Summary

In this article, 16 years of SABER mesosphere temperature profiles are utilized to investigate the MIL phenomenon and its causative mechanism through gravity wave potential energy (P_E) and instability criteria of Bruent-Vaisala frequency (N^2) over low latitude bands. The observational conclusions from this chapter are drawn as follows:

- ✓ The occurrence rate of the upper mesosphere inversion frequency is maximum relative to the mean occurrence rate of the lower mesosphere inversions.
- ✓ Based on the analysis of frequency of occurrence on mesospheric inversion layer (MIL) characteristic features, it is revealed that the most probable value for upper inversion amplitude is 38 k with standard deviations (SD) of 1.72 k, inversion layer thicknesses are 5.5 km with SD of 2.3 km, and the base height is 78 km with an SD of 2.8 km. Whereas the lower inversion amplitude is 25 K with an SD of 14.5 K, the inversion layer thickness is 3.8 km with an SD of 1.72 km and a base height of 73 km with an SD of 2.07 km.
- ✓ The gravity wave indicator potential energy depicts high energy at the upper mesosphere region compared to the lower mesosphere region.

- ✓ The result concludes that the observation of high potential energy in the upper mesosphere region is due to the deposition of high energy and momentum at the background temperature by gravity wave breaking, which could influence the dynamics of the inversion phenomenon
- ✓ The stability criteria at the mesosphere region are indicated by Brunt-Vaisala frequency (N^2), which shows low values at the upper mesosphere region relative to the lower mesosphere region, leading to the conclusion that the high potential energy at the upper mesosphere region is due to the instability over that region, which gives rise to large inversion phenomena.
- ✓ In general, we concluded that the processes in the atmosphere vary from region to region. As a result, the atmospheric state varies significantly with altitude as well as from place to place and time to time.

Data availability. The SABER data are freely available via the link at http://saber.gats-inc.com/index.php.

Author contribution. Chalachew Lingerew: data curation, investigation, software, visualization, writing the original draft, and writing review. U. Jaya Prakash Raju; supervision, and editing.

Competing interest. The authors declare that they have no conflict of interest relevant to this study.

Acknowledgments. The Authors would like to express their gratitude to the National Aeronautics and Space Administration (NASA) for providing the SABER data downloaded from the website: http://saber.gats-inc.com/index.php.

References

Begue, N., Mbatha, N., Bencherif, H., Loua, R. T., Siva Kumar, V., & Leblanc, T.: Statistical analysis of the mesospheric inversion layers over two symmetrical tropical sites: Reunion (20.8° S, 55.5° E) and Mauna Loa (19.5° N, 155.6° W). *In Annales Geophysicae*, 35, 1177-1194, 2017.

Bizuneh, C.L., Prakash, R., and Nigussie, M.: Long-term temperature and ozone response to natural drivers in the mesospheric region using 16 years (2005–2020) of TIMED/SABER observation data at 5-15^{0}N. Advances in Space Research, 70, 2095–2111, https://doi.org/10.1016/j.asr.2022.06.051, 2022.

Collins, R. L., Lehmacher, G. A., Larsen, M. F., and Mizutani, K.: Estimates of vertical eddy diffusivity in the upper mesosphere in the presence of a mesospheric inversion layer, Ann. Geophys., 29(11), 2019–2029, http://doi:10.5194/angeo-29-2019-2011, 2011.

Cutler, L. J., Collins, R. L., Mizutani, K., and Itabe, T.: Rayleigh lidar observations of mesospheric inversion layers at Poker Flat, Alaska (65^0 N, 14^0 W), Geophys. Res. Lett., 28, 1467–1470, https://doi.org/10.1029/2000GL012535, 2001.

Duck, T. J., Sipler, D. P., and Salah, J. E.: Rayleigh lidar observations of a mesospheric inversion layer during night and day, Geophys. Res. Lett., 28, 3597–3600, 2001.

Duck, T. J. and Greene, M. D.: High Arctic observations of mesospheric inversion layers, Geophys. Res. Lett., 31, L02105, https://doi.org/10.1029/2003GL018481, 2004.

Eckermann, S.D., Hirota, I., and Hocking, W. K.: Gravity wave and equatorial wave morphology of the stratosphere derived from long-term rocket soundings. Q. J. R. Meteorol. Soc., 121, 149 186, http://doi.org/10.1002/qj.49712152108, 1994.

Emanuel, K.A.: Atmospheric Convection, Oxford University Press, New York, 580pp, 1994.

Fechine, J., Wrasse, C. M., Takahashi, H., Mlynczak, M. G., and Russell, J. M.: Lower-mesospheric inversion layers over Brazilian equatorial region using TIMED/SABER temperature profiles, Adv. Space Res., 41, 1447–1453, https://doi.org/10.1016/j.asr.2007.04.070, 2008.

Fritts, D. C., Wang, L., Laughman, B., Lund, T. S., & Collins, R. L.: Gravity wave dynamics in a mesospheric inversion layer: 2. Instabilities, turbulence, fluxes, and mixing. Journal of Geophysical Research: Atmospheres, 123, 649–670, https://doi.org/10.1002/2017JD027442, 2018.

Fritts, D. C., and Alexander, M. J.: Gravity wave dynamics and effects in the middle atmosphere, Rev. Geophys., 41, 1003, https://doi.org/10.1029/2001RG000106, 2003.

Fritts, D. C., Laughman, B., Wang, L., Lund, T. S., & Collins, R. L.: Gravity wave dynamics in a mesospheric inversion layer: 1. Reflection, trapping, and instability dynamics. Journal of Geophysical Research: Atmospheres, 123, 626-648, https://doi.org/10.1002/2017JD027440, 2018.

Gan, Q., Zhang, S. D., and Yi, F.: TIMED/SABER observations of lower mesospheric inversion layers at low and middle latitudes, J. Geophys. Res., 117, D07109, https://doi:0.1029/2012JD 017455, 2012.

Garcia-Comas, M., Lopez-Puertas, M., Marshall, B. T., Winter Steiner, P. P., Funke, B., Bermejo-Pantaleon, D., Mertens, C. J., Remsberg, E. E., Gordley, L. L., Mlynczak, M. G., and Russell III,

J. M.: Errors in Sounding of the Atmosphere using Broadband Emission Radiometry (SABER) kinetic temperature caused by non-local-thermodynamic-equilibrium model parameters, J. Geophys. Res., 113, D24106, doi: 10.1029/2008JD010105, 2008.

Hirota, I.: Climatology of gravity waves in the middle atmosphere. J. Atmos. Terr. Phys., 46, 767–773, http://doi.org/10.2151/jmsj1965.63.6-1055, 1984.

Hamilton, K.: Climatological Statistics of Stratospheric Inertia-Gravity Waves Deduced from Historical Rocket-sonde Wind and Temperature Data. J. Geophys. Res., 96, 20831–20839, http://doi.org/10.1029/91JD02188, 1991.

Hauchecorne, A., Chanin, M. L., & Wilson, R.: Mesospheric temperature inversion and gravity wave breaking. *Geophysical Research Letters*, 14(9), 933-936, https://doi.org/10.1029/GL014i009p00933, 1987.

Holton, J. R., Curry, J. A., and Pyle, J. A.: *Encyclopedia of atmospheric sciences*, volume 1. Academic Press, 2003.

Holton, J. R.: The influence of gravity wave breaking on the general circulation of the middle atmosphere, J. Atmos. Sci., 40, 2497–2507, 1983.

Holton, J. R. and Hakim, G. J.: *An introduction to dynamic meteorology*. Academic Press, 2013.

Irving, B. K., Collins, R. L., Lieberman, R. S., Thurairajah, B., and Mizutani, K.: Mesospheric Inversion Layers at Chatanika, Alaska (65°N, 147°W): Rayleigh lidar observations and analysis, J. Geophys. Res. Atmos., 119, 11,235–249, http://doi:10.1002/2014JD021838, 2014.

John, S.R., Kumar, K. K.: TIMED/SABER observations of global gravity wave climatology and their interannual variability from stratosphere to mesosphere lower thermosphere. Clim. Dyn., 39, 1489–1505, http://doi.org/10.1007/s00382-012-1329-9, 2012.

Leblanc, T., McDermid, I. S., Hauchecorne, A., and Keck hut, P.: Evaluation of optimization of lidar temperature analysis algorithms using simulated data, J. Geophys. Res., 103, 6177–6187, 1998.

Leblanc, T., and Hauchecorne, A.: Recent observations of mesospheric temperature inversions, J. Geophys. Res., 102, 19471–19482, https://doi.org/10.1029/97JD01445, 1997.

Lindzen, R. S.: Turbulence and stress due to gravity waves and tidal breakdown, J. Geophys. Res., 86, 9707–9714, https://doi:10.1029/JC086iC10p09707, 1981.

Lingerew, C., Jaya Prakash Raju, U., & Guimarães Santos, C. A.: NN-MLT model prediction for low-latitude region based on artificial neural network and long-term SABER observations. *Earth and Space Science*, *10*, e2023EA002930, https://doi.org/10.1029/2023 EA002930, 2023.

Liu, S-D., and S-S. Liu: *Atmosphere Dynamics*, Peking University Press, Beijing, 2011.

Liu, H. L., Hagan, M. E., & Roble, R. G.: Local mean state changes due to gravity wave breaking modulated by the diurnal tide. *Journal of Geophysical Research*, 105(D10), 12381-12396, (2000).

Liu, H. L., & Hagan, M. E.: Local heating/cooling of Atmospheres. 96(D8), 15297-15309, (1998).

Mlynczak, M. G., Marshall, B. T., Martin-Torres, F. J., Russell III, J. M., Thompson, R. E., Remsberg, E. E., and Gordley, L. L.: Sounding of the Atmosphere using Broadband Emission Radiometry observations of daytime mesospheric O_2 (1Δ) 1.27 μm emission and derivation of ozone, atomic oxygen, and solar and chemical energy deposition rates, 2007.

Meriwether, J. W., and Gerrard, A. J.: Mesosphere inversion layers and stratosphere temperature enhancements, Rev. Geophys., 42, RG3003, http//doi:10.1029/2003RG000133, 2004.

Meriwether, J. W., and Gardner, C. S.: A review of the mesosphere inversion layer phenomenon, J. Geophys. Res., 105, 12 405–12 416, 2000.

Nath, O., & Sridharan, S.: Long-term variabilities and tendencies in zonal mean TIMED–SABER ozone and temperature in the middle atmosphere at 10–15°N. Journal of Atmospheric and Solar-Terrestrial Physics, 120, 1–8, https://doi:10.1016/j.jastp.2014.08.010, 2014.

Ramesh, K., Sridharan, S.: Large mesospheric inversion layer due to breaking of small scale gravity waves: Evidence from Rayleigh lidar observations over Gadanki (13.51^0 N, 79.21^0 E). J. Atmos. Sol. Terr. Phys. 89, 90–97, http://doi.org/10.1016/j.jastp.2012.08.011, 2012.

Ramesh, K., Sridharan, S. and Vijaya Bhaskara, S.: Causative mechanisms for the occurrence of a triple-layered mesospheric inversion event over low latitudes, J. Geophys. Res. Space Physics, 119, 3930–3943, http://doi:10.1002/2013JA019750, 2014.

Ramesh, K., Sridharan, S., Raghunath, K., and Rao, S. V. B.: A chemical perspective of day and night tropical (10°N–15°N) mesospheric inversion layers, J. Geophys. Res. Space Physics, 122, http://doi:10.1002/2016JA023721, 2017.

Ramesh, K., Sridharan, S., Vijaya Bhaskara Rao, S., Raghunath, K., Bhavani Kumar, K.: Rayleigh lidar observations of mesospheric inversion layers over Gadanki (13.5^0N, 79.2^0 E) and their relation with gravity wave activities. Indian Journal of Radio and Space Science, 43, 83-90, 2013.

Remsberg, E., Lingenfelser, V., Harvey, V., Grose, W., Russell III, J., Mlynczak, M., Gordley, L., and Marshall, B. T.: The verification of the quality of SABER temperature, geopotential height,

and wind fields by comparison with Met Office assimilated analyses, J. Geophys. Res., 108(D19), 4628, https://doi:10.1029/2003JD003720, 2003.

Rezac, L., Kutepov, A., Russell, J.M., Feofilov, A.G., Yue, J., and Goldberg, R.A.: Simultaneous retrieval of T (p) and CO2 VMR from two-channel non-LTE limb radiances and application to daytime SABER/ TIMED measurements. J. Atmos. Sol. Terr. Phys 130–131, 23–42. https://doi.org/10.1016/j.jastp.2015.05.004, 2015.

Russell, J.M., Mlynczak, M.G., Gordley, L.L., Tansock, J., Esplin, R.: An overview of the SABER experiment and preliminary calibration results. In Proceedings of the SPIE, 44th Annual Meeting, Denver, CO, USA, 3756, 277–288, 1999.

Schmidlin, F. J.: Temperature inversions near 75 km. *Geophysical Research Letters*, 3(3), 173-176, (1976).

Sica, R. J., Argall, P. S., Shepherd, T. G., and Koshyk, J. N.: Model-measurement comparison of mesospheric temperature inversions, and a simple theory for their occurrence, Geophys. Res. Lett., 34, L23806, https://doi:10.1029/2007GL030627, 2007.

Sivakandan, M., Kapasi, D., and Taori, A.: The occurrence altitudes of middle atmospheric temperature inversions and mesopause over low-latitude Indian sector, Ann. Geophys., 32, 967–974, https://doi.org/10.5194/angeo-32-967-2014, 2014.

Siva Kumar, V., Bhavani Kumar, Y., Raghunath, K., Rao, P. B., Krishnaiah, M., Mizutani, K., Aoki, T., Yasui, M., and Itabe, T.: Lidar measurements of mesospheric temperature inversion at a low latitude, Ann. Geophys., 19, 1039–1044, https://doi.org/10.5194/angeo-19-1039-2001, 2001.

Sridharan, S., Sathishkumar, S., and Gurubaran, S.: Influence of gravity waves and tides on mesospheric temperature inversion layers: simultaneous Rayleigh lidar and MF radar observations, Ann. Geophys., 26, 3731–3739, 2008.

Singh, R. P., & Pallamraju, D.: Mesospheric temperature inversions observed in OH and O2 rotational temperatures from Mount Abu (24.6°N, 72.8°E), India. Journal of Geophysical Research: Space Physics, 123, 8823–8834, https://doi.org/10.1029/2018JA025703, 2018.

Smith, A.: Global Dynamics of the MLT, Surv. Geophys, 33, 1177–1230, https://doi.org/10.1007/s10712-012-9196-9, 2012.

Szewczyk, A., Strelnikov, B., Rapp, M., Strelnikova, I., Baumgarten, G., Kaifler, N., Dunker, T., and Hoppe, U. P.: Simultaneous observations of a Mesospheric Inversion Layer and turbulence

during the ECOMA-2010 rocket campaign, Ann. Geophys., 31, 775–785, http://doi:10.5194/angeo-31-775-2013, 2013.

Vadas, S. L., and Fritts, D. C.: Thermosphere responses to gravity waves: Influences of increasing viscosity and thermal diffusivity, J. Geophys. Res., VOL. 110, D15103, doi: 10.1029/2004JD 005574, 2005.

Wang, L., Geller, M.A., Alexander, M.J.: Spatial and Temporal Variations of Gravity Wave Parameters. Part I: Intrinsic Frequency, Wavelength, and Vertical Propagation Direction. J. Atmos. Sci., 62, 125–142, http://doi.org/10.1029/2010JD013860, 2005.

Wang, L., and Alexander, M.J.: Global estimates of gravity wave parameters from GPS radio occultation temperature data. J. Geophys.Res. 115, D21122, http://doi.org/10.1029/2010J D013860, 2010.

Walterscheid, R. L., and Hickey, M. P.: Gravity wave ducting in the upper mesosphere and lower thermosphere duct system, J. Geophys. Res., 114, D19109, http://doi:10.1029/2008JD 011269, 2009.

Yuan, T., Pautet, P. D., Zhao, Y., Cai, X., Criddle, N. R., Taylor, M. J., and Pendleton, W. R.: Coordinated investigation of mid-latitude upper mesospheric temperature inversion layers and the associated gravity wave forcing in Logan, Utah, J. Geophys. Res. Atmos., 119, 3756–3769, http://doi:10.1002/2013JD020586, 2014.